Progress in Oceanography 170 (2019) 93–106

Contents lists available at ScienceDirect

Progress in Oceanography

journal homepage: www.elsevier.com/locate/pocean

Dissolved organic matter (DOM) in the open Mediterranean Sea. II: Basin–wide distribution and drivers of fluorescent DOM

Alba María Martínez–Pérez[a,*], Teresa S. Catalá[a,b,c], Mar Nieto–Cid[a,d], Jaime Otero[a], Marta Álvarez[d], Mikhail Emelianov[e], Isabel Reche[b], Xosé Antón Álvarez–Salgado[a], Javier Arístegui[f]

[a] CSIC Instituto de Investigacións Mariñas, Vigo, Spain
[b] Departamento de Ecología and Instituto del Agua, Universidad de Granada, Granada, Spain
[c] Research Group for Marine Geochemistry, Institute for Chemistry and Biology of the Marine Environment (ICBM), Carl von Ossietzky University, Oldenburg, Germany
[d] IEO Centro Oceanográfico de A Coruña, Coruña, Spain
[e] CSIC Institut de Ciències del Mar, Barcelona, Spain
[f] Institute of Oceanography and Global Change (IOCAG), Univ. Las Palmas de Gran Canaria, Telde, Las Palmas, Canary Islands, Spain

ARTICLE INFO

Keywords:
Dissolved organic matter
Fluorescence spectroscopy
PARAFAC
Water mass analysis
Mediterranean Sea

ABSTRACT

Fluorescent dissolved organic matter (FDOM) in the Mediterranean Sea was analysed by excitation–emission matrix (EEM) spectroscopy and parallel factor (PARAFAC) analysis during the cruise HOTMIX 2014. A 4–component model, including 3 humic–like and 1 protein–like compounds, was obtained. To decipher the environmental factors that dictate the distributions of these components, we run generalized additive models (GAMs) in the epipelagic layer and an optimum multiparametric (OMP) water masses analysis in the meso– and bathypelagic layers. In the epipelagic layer, apparent oxygen utilization (AOU) and temperature presented the most significant effects on the variability of the marine humic-like peak M fluorescence, suggesting that its distribution was controlled by the net community respiration of organic matter and photobleaching. On the contrary, the variability of the soil humic-like peak E and the protein–like peak T fluorescence was explained mainly by the prokaryotic heterotrophic abundance, which decreased eastwards. In the meso– and bathypelagic layers, water mass mixing and basin–scale mineralization processes explained > 72% and 63% of the humic–like and protein–like fluorescence variability, respectively. When analysing the two basins separately, the OMP model offered a better explanation of the distribution of fluorescence in the eastern Mediterranean Sea, as expected from the reduced biological activity in this ultra–oligotrophic basin. Furthermore, while western Mediterranean deep waters display the usual trend in the global ocean (increase of humic–like fluorescence and decrease of protein–like fluorescence with higher AOU values), the eastern Mediterranean deep waters presented an opposite trend. Different initial fluorescence intensities of the water masses that mix in the eastern basin, with Adriatic and Aegean origins, seem to be behind this contrasting pattern. The analysis of the transect–scale mineralization processes corroborate this hypothesis, suggesting a production of humic–like and a consumption of protein–like fluorescence in parallel with water mass ageing. Remarkably, the transect–scale variability of the chromophoric dissolved organic matter (CDOM) absorbing at the excitation wavelength of the humic–like peak M indicates an unexpected loss with increasing AOU, which suggests that the consumption of the non–fluorescent fraction of CDOM absorbing at that wavelength exceeded the production of the fluorescent fraction observed here.

1. Introduction

This manuscript is part of a broader study about the environmental drivers of the optically active fraction of dissolved organic matter (DOM) in the open waters of the Mediterranean Sea, hereinafter MedSea. The chromophoric fraction of DOM (CDOM) has been examined in the companion study by Catalá et al. (2018), who explored the physical and biogeochemical drivers that dictate the distributions of CDOM absorption coefficients and spectral slopes in epi–, meso–, and bathypelagic waters of the MedSea. Here we focus on the small fraction

* Corresponding author.
E-mail address: albam@iim.csic.es (A.M. Martínez–Pérez).

https://doi.org/10.1016/j.pocean.2018.10.019
Received 22 November 2017; Received in revised form 21 October 2018; Accepted 31 October 2018
Available online 02 November 2018
0079-6611/

of this CDOM pool that is able to emit the light absorbed in the form of blue fluorescence, i.e. on the fluorescent dissolved organic matter (FDOM) pool.

FDOM consist basically on two groups of fluorophores: protein–like substances, related mainly to the aromatic amino–acids tyrosine and tryptophan, which absorb at < 300 nm; and humic–like substances, related to terrestrial and marine humic and fulvic acids, which absorb at > 300 nm (Coble, 2007; Nelson and Siegel, 2013; Coble et al., 2014; Stedmon and Nelson, 2015). FDOM is reliably, fast and easily determined by fluorescence spectroscopy, being widely used over the last decade to gain fundamental knowledge on the impact of ocean circulation, mixing and biogeochemical processes on DOM cycling in open ocean waters (Yamashita and Tanoue, 2008; Jørgensen et al., 2011; Catalá et al., 2015a; Nelson and Gauglitz, 2016; Yamashita et al., 2017).

While the dynamics of dissolved organic carbon (DOC) in the open MedSea is well-known (Santinelli, 2015 and the references therein), FDOM studies have been mostly conducted in coastal areas (Para et al., 2010; Romera-Castillo et al., 2013; Sánchez-Pérez et al., 2016; Aparicio et al., 2017) and local seas (Zeri et al., 2014, Gonnelli et al., 2016, Cyr et al., 2017; Pitta et al., 2019) of the MedSea. However, the basin–wide distribution of FDOM in the open MedSea remains largely unknown yet. The particular hydrography and circulation of the MedSea with its large variety of water masses despite its small size (Bergamasco and Malanotte-Rizzoli, 2010; Catalá et al., 2018), its reduced renewal times of decades vs. centuries for the global ocean (Laruelle et al., 2009; Schneider et al., 2014; Powley et al., 2016), and its relatively high deep water temperatures of about 13 °C vs. < 3 °C in the global ocean (Dickson and Brown, 1994) makes this "miniature ocean" very suitable for biogeochemical studies in general, and the fluorescent fraction of CDOM in particular.

Here, we hypothesize that the distribution of the different FDOM fractions in the open waters of the MedSea is dictated by the origin of the materials (terrestrial vs. marine), the formation area of the intermediate and deep water masses (Eastern vs. Western, Adriatic vs. Aegean), and the microbial and photochemical transformations experienced during their transit through the MedSea. As for the case of the companion paper by Catalá et al. (2018), the aim of this study is to assess whether the distribution and environmental drivers (physical vs. biogeochemical, photochemical vs. microbial, autotrophic vs. heterotrophic) of FDOM in the MedSea differs from the world ocean and whether the contrasting degree of oligotrophy between the WestMed and the EastMed affects the dynamics of FDOM. To do so, PARAFAC analysis (Stedmon and Bro, 2008) is used to identify the main fluorophores present in the MedSea. General additive models (GAMs) are used to explore the environmental drivers of the FDOM fluorophores in the epipelagic layer. In the meso– and bathypelagic layers, an optimum multiparameter (OMP) water mass analysis is used to differentiate the effect of water mass mixing from the biogeochemical processes occurring during this mixing, on the variability of FDOM. Furthermore, the OMP analysis also allowed us to obtain a census of the main fluorophores in all the water masses intercepted during the cruise.

2. Materials and methods

2.1. Sampling strategy

Twenty–four hydrographic stations were sampled across the entire MedSea from the Levantine Basin to the Strait of Gibraltar (Fig. 1) during the HOTMIX 2014 cruise, on board the R/V Sarmiento de Gamboa (Heraklion, Crete, 27 April 2014 – Las Palmas, Canary Islands, 29 May 2014). A description of the sampling strategy, core measurements, GAMs and OMP water mass analysis is included below.

At each station, water samples were taken from surface to bottom (max. 15 levels) using a SBE 38 rosette sampler, equipped with 24 (12 L) Niskin bottles. Two conductivity, temperature and depth probes (CTD SBE 911 plus), dissolved oxygen (SBE–43 oxygen sensor) and fluorescence of chlorophyll *a* (SeaPoint fluorometer) sensors were attached to the rosette sampler. Discrete sampling depths were decided according to the values of the continuous profiles of potential temperature (θ), salinity (S), dissolved oxygen (O_2) and fluorescence of chlorophyll *a* (Chl *a*). A total of 330 samples were collected during the cruise.

Seawater samples were collected to analyse salinity (S), dissolved oxygen (O_2) and Chlorophyll *a* (Chl *a*) to calibrate the sensors for conductivity, O_2 and fluorescence of Chl *a*, respectively. In addition, inorganic nutrients and prokaryotic heterotrophic abundance (PHA) were also determined in all samples (see Section 2.2).

Samples for the determination of fluorescent dissolved organic matter (FDOM) were collected in 0.5–litres acid–cleaned glass bottles. Discrete samples collected at < 200 m were filtered through precombusted (450 °C, 4 h) Whatman GF/F filters with an acid–cleaned all–glass filtration system under positive pressure of high–purity N_2, previously rinsing with about 50 mL of the sample. Dark ocean samples were not filtered. FDOM aliquots were kept in the dark until analysis on board by fluorescence spectroscopy (see Section 2.3) within two hours of collection.

2.2. Determination of explanatory variables

Salinity samples were measured on board with a Guildline Portasal salinometer Model 8410A. Conductivity measurements were converted into practical salinity scale values with the equation of UNESCO (1985). Dissolved oxygen was determined on board following the Winkler method with potentiometric endpoint as modified after Langdon (2010). The apparent oxygen utilization ($AOU = O_{2sat} - O_2$) was calculated using the algorithm proposed by Benson & Krause (UNESCO, 1986) for oxygen saturation (O_{2sat}). Chl *a* concentration was determined on board after filtration of 0.5 L of seawater through a GF/F filter and storage frozen until analysis. Pigments were extracted in cold acetone (90% v/v) for 24 h and analyzed with a 10 AU Turner Designs bench fluorometer, calibrated with pure Chl a (Sigma Aldrich), according to Holm-Hansen et al. (1965). Nitrate, phosphate and silicate concentrations were determined using a Skalar segmented flow autoanalyzer SAN + + following the colorimetric methods of Grasshoff et al. (1999). The heterotrophic prokaryote abundance (PHA) was measured by flow cytometry. Samples (1.6 mL) were preserved with paraformaldehyde (2% final concentration), left 15 min at 4 °C in the dark to fix, deep frozen in liquid nitrogen and stored at −80 °C until analysed. The day after, subsamples (400 µL) were stained with the fluorochrome SYBR Green I, Molecular Probes (final concentration 1000× dilution of the commercial product) at room temperature before analyses at low speed (< 20 µL min^{-1}) with a BD FACSCalibur cytometer, fitted with a 15 mW laser emitting at 488 nm. Cells were identified in bivariate plots of side scatter (SSC–H) *versus* green fluorescence (FL1–H). A suspension of yellow–green 1 µm latex beads (~10^6 beads mL^{-1}) was added as an internal standard (Polysciences, Inc.).

2.3. Determination of the response variables: FDOM matrices and PARAFAC processing

Fluorescence excitation–emission matrices (EEMs) were collected with a JY–Horiba Spex Fluoromax–4 spectrofluorometer at room temperature (around 20 °C) using 5 nm excitation and emission slit widths, an integration time of 0.25 s, an excitation range of 240–450 nm at 10 nm increments and an emission range of 300–560 nm at 2 nm increments. To correct for lamp spectral properties and to compare results with those reported in other studies, spectra were collected in signal–to–reference (S:R) mode with instrument–specific excitation and emission corrections applied during collection, and EEMs were normalized to the Raman area (RA). In our case, the RA and its baseline correction were performed with the emission scan at 350 nm of the Milli–Q water blanks and the area was calculated following the

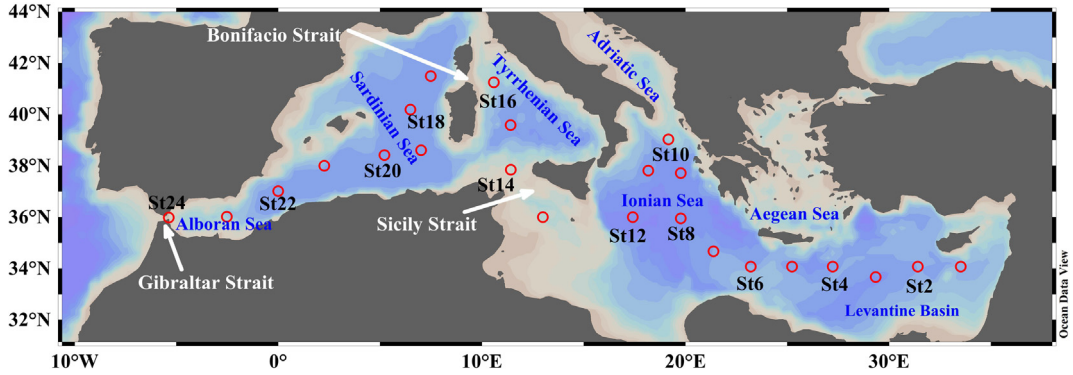

Fig. 1. Map of the study area and hydrographic stations occupied during the HOTMIX 2014 cruise. White arrows indicate the main straits of the MedSea. Figure created using the software ODV.

trapezoidal rule of integration (Murphy et al., 2010). Rayleigh scatter bands were removed mathematically from the EEMs.

To track the variability of the instrument in the Raman, protein– and humic–like regions of the spectrum and to assess gradual spectral bias during the 33 working days of the cruise, three standards were run daily: (1) a p–terphenyl block (Starna) that fluoresces in the protein region, between 310 and 600 nm exciting at 295 nm; (2) a tetraphenyl butadiene block (Starna) that fluoresces in the humic region, between 365 and 600 nm exciting at 348 nm; and (3) a sealed Milli–Q cuvette (Perkin Elmer) scanned between 365 and 450 nm exciting at 350 nm. Fig. S1a in the supplementary material shows that the temporal evolution of the RA of the Milli–Q water produced on board and the reference p–terphenyl and tetraphenyl butadiene materials were parallel, which confirms that the Raman normalization was successful in both the protein– and the humic–like regions of the EEMs. Therefore, no additional drift corrections were necessary. In addition, sealed Milli-Q reference cuvette and daily Milli-Q water produced on board showed similar pattern of evolution during the cruise, indicative of a good quality of the Milli-Q water produced in the ship (Fig. S1b). Furthermore, two scans of the reference sealed Milli-Q water were measured at the beginning (sMQ1) and at the end (sMQ2) of each session, which reveals a slight decrease of the fluorescence intensities along each working day (Fig. S1c). The initial and final sMQ spectra were separated about 8 h of continuous work of the spectrofluorometer. We found that the difference between sMQ1 and sMQ2 was only 0.69%. Raman–normalized Milli–Q blanks were subtracted to remove the Raman scattering signal (Stedmon et al., 2003; Murphy et al., 2010). RA normalization, blank subtraction and generation of EEMs were performed using Matlab (version R2014B).

A Parallel factor analysis (PARAFAC) was then applied to decompose the fluorescence signal of the EEMs into the underlying individual fluorescent components (Bro, 1997). The PARAFAC was based on 406 corrected EEMs and was performed using the DOMFluor 1_7 Toolbox8 (Stedmon and Bro, 2008) and Matlab (version R2014B). Before validating the model, only 3 outliers were withdrawn from the database. A 4–component model was obtained (Fig. 2) after split–half validation and random initialization steps (Stedmon and Bro, 2008; Murphy et al., 2013). PARAFAC analysis was exclusively used to identify the main fluorophores in the data set.

Furthermore, from the original EEMs we picked up specific values at selected excitation–emission wavelength pairs previously defined by Coble (1996) and Stedmon et al. (2003). The selected Ex/Em wavelength pairs were 250 nm/435 nm (peak A) due to general humic substances; 340 nm/440 nm (peak C) due to humic substances of terrestrial origin; 320 nm/410 nm (peak M) due to humic substances of marine origin; 450 nm/520 nm (peak E) due to soil fulvic acids; and 280 nm/350 nm (peak T) and 270 nm/304 nm (peak B) due to protein–like substances, tryptophan and tyrosine–like respectively. Fluorescence intensities of these peaks are reported in Raman units (RU).

Simple linear regression between fluorescence peaks was calculated using Pearson's correlation.

2.4. Generalized additive models (GAMs)

To test for the degree of relationship between the environmental parameters (inorganic nutrients, O_2, AOU, Chl *a* and PHA) and the distribution of the FDOM fluorophores in the epipelagic layer of the MedSea we have used generalized additive models (GAMs, Wood, 2006). A GAM is a nonparametric regression technique that allows inspecting the relationship between a response variable and one (or more) continuous explanatory variable(s) without the need to choose a particular parametric form for describing the shape of the relationship (s). In this study, the explanatory variables are the environmental parameters and the response variables are the FDOM fluorophores. Before model fitting, covariability among all potential predictors was examined using pairwise correlations and calculating variance inflation factors (VIFs, Table S1). The VIF analysis selected the following variables: θ, AOU, Chl *a* and PHA. GAMs were formulated as follows:

$$Y_{i,l} = \alpha + \sum_j g_j(X^j{}_{i,l}) + \in_{i,l} \quad (1)$$

where Y is the FDOM fluorophores (peak A, C, M, E and T) measured at a station i and depth level l, α is an intercept, X is a vector of predictor variables where the superscript j identifies each covariate, g is a non–parametric smoothing function specifying the effect of each covariates on the response variables and $\in_{i,l}$ is the error term assumed to be normally distributed. Smoothing functions were fit by penalized cubic regression splines restricted to a maximum of three knots. The smoothness of the functions was estimated by minimizing the generalized cross validation criterion. All models were fitted in R 3.2.3 software (R Development Core Team, 2016) and using the 'mgcv 1.8–16' package (Wood, 2006).

2.5. Optimum multiparameter (OMP) water mass analysis

Despite the small size of the MedSea, a total of 19 water types were identified along the HOTMIX 2014 cruise track (see Table 1 in Catalá et al., 2018). A water type is a unique combination of physical and biogeochemical tracers, in our case potential temperature (θ), salinity (S), silicate (SiO_4) and the conservative parameter NO ($=O_2 + R_N\ NO_3$; with $R_N = 9.3$ mol O_2 mol N^{-1}; following Anderson, 1995). The OMP allows computing the optimum contribution of each water type to every water parcel/sample by solving over–determined systems of linear mixing equations for volume, θ, S, SiO_4 and NO in a non-negative less–squares sense (Tomczak and Large, 1989). For further details see the companion study of Catalá et al. (2018). In the Western Mediterranean, hereafter WestMed, the shallowest water type was the Atlantic Water (AW) that enters the MedSea across the Strait of

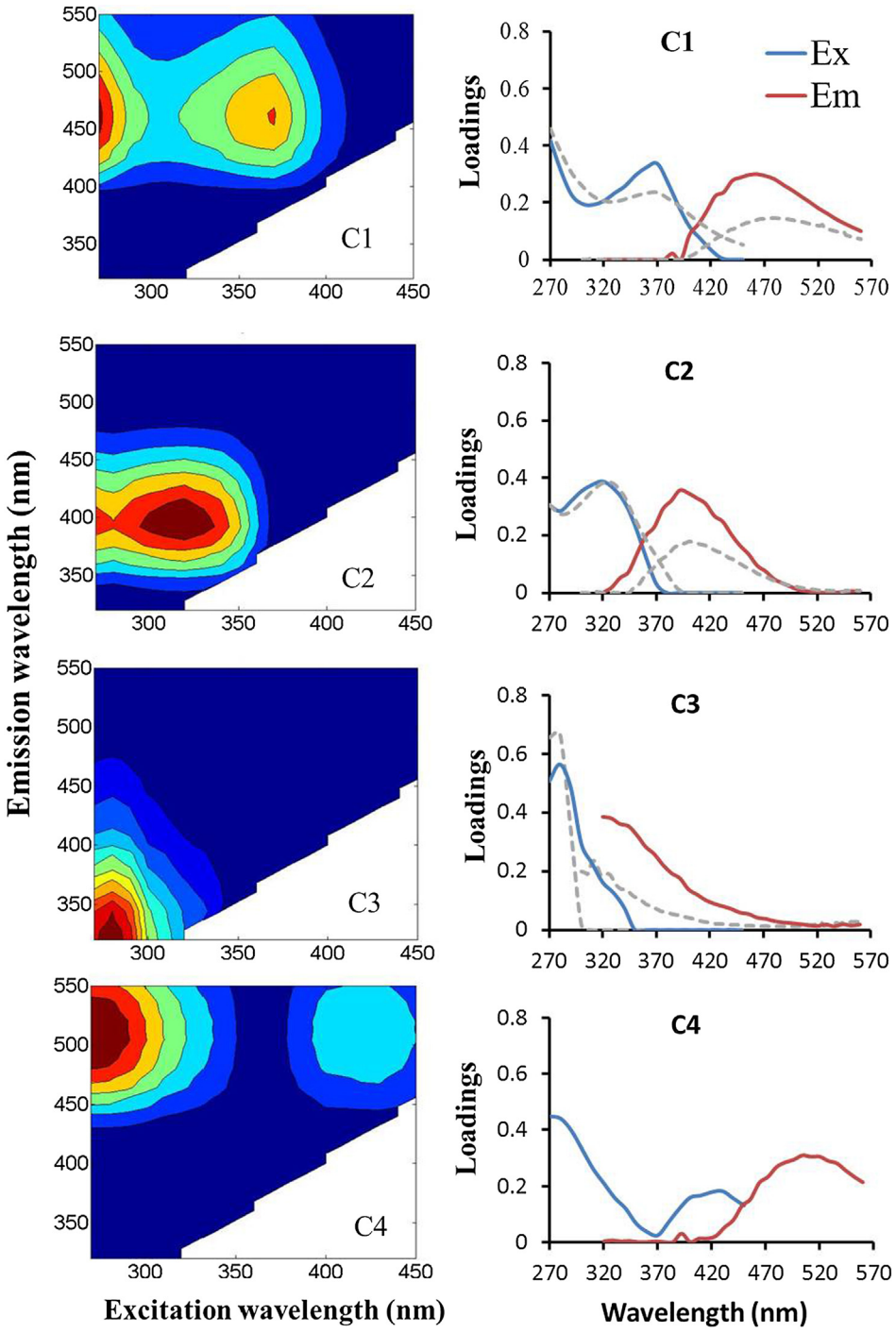

Fig. 2. Fluorescence matrices of the four identified PARAFAC components. C1 represents a combination of Coble's (1996) peaks A and C, C2 represents peak M, C3 corresponds to a mixture of peak T and peak B and C4 represents Stedmon et al. (2003) peak E. The right panels represent the excitation (blue lines) and the emission (red lines) fluorescence intensities of the four PARAFAC components, which are compared with the PARAFAC components found in the global ocean (dashed grey lines) by Catalá et al. (2015a). Figure created using the software Matlab (version R2014B; MathWorks, USA). (For interpretation of the references to colour in this figure legend, the reader is referred to the web version of this article.)

Gibraltar. The Winter Intermediate Water (WIW) is located below the AW, and it is formed in the slope of the Gulf of Lions and the Balearic Sea. The Eastern Intermediate Water (EIW), coming from the Eastern Mediterranean, enters the basin through the Strait of Sicily. The deep WestMed is filled with up to five varieties of Western Mediterranean Deep Water (WMDW) formed by deep convection in the Gulf of Lions (see Table 1b and Fig. 3 in Catalá et al., 2018). In the Eastern Mediterranean, hereafter EastMed, two surface waters have to be considered: Modified Atlantic Water (MAW) at the Strait of Sicily and Levantine Surface Water (LSW) in the Levantine basin. The intermediate layer is occupied by the Levantine (LIW) and Cretan (CIW) intermediate waters. In the deep layer five varieties of the Eastern Mediterranean Deep Water (EMDW) are found, one of Aegean origin and four of Adriatic origin, occupying different depth ranges in the Ionian and Levantine basins (see Table 1a and Fig. 3 in Catalá et al., 2018).

Using the values of any measured variable (N) and the proportions of the 19 water masses identified in this study (x_{ij}), the water mass proportion–weighted average concentration of N in each water type, N_i, herein after archetype value of N, can be calculated as:

$$N_i = \frac{\sum_j x_{ij} \cdot N_j}{\sum_j x_{ij}} \quad (2)$$

where N_i is the archetype value of N in water mass *i*; N_j is the value of N in sample j; and x_{ij} is the proportion of water mass *i* in sample j.

To determine the fraction of the total variability of variable N that is due to water mass mixing, a multiple linear regression of N_j with the

Table 1
Archetypal depth (Z_i, m), apparent oxygen utilization (AOU_i, μmol kg^{-1}), peak A_i (10^{-3} RU), peak C_i (10^{-3} RU), peak M_i (10^{-3} RU), peak T_i (10^{-3} RU), peak E_i (10^{-4} RU) (%), of the water mass intercepted during the HOTMIX cruise. VOL_i, (%) represents the percentage of the total volume of water sampled that corresponded to each water mass.

	Acronym	VOL_i	Z_i	AOU_i	Peak A_i	Peak C_i	Peak M_i	Peak T_i	Peak E_i
EastMED	MAW	3.2	125 ± 26	13 ± 5	14.0 ± 0.7	5.4 ± 0.3	7.1 ± 0.4	7.4 ± 0.6	5.5 ± 0.7
	LSW	1.8	116 ± 21	3 ± 3	11.3 ± 0.6	4.3 ± 0.3	5.5 ± 0.3	7.6 ± 0.8	3.9 ± 0.5
	LIW	12.2	149 ± 13	15 ± 2	13.6 ± 0.4	5.3 ± 0.2	6.9 ± 0.2	7.5 ± 0.3	4.9 ± 0.4
	CIW	6.6	379 ± 56	47 ± 3	15.4 ± 0.4	6.4 ± 0.1	8.0 ± 0.2	6 0.0 ± 0.7	8.2 ± 0.5
	AdMW	5.8	273 ± 55	34 ± 5	15.6 ± 0.4	6.2 ± 0.2	7.9 ± 0.2	6.7 ± 0.6	6.8 ± 0.7
	AdDW	0.5	1425 ± 403	59 ± 4	14.5 ± 0.5	6.1 ± 0.2	7.3 ± 0.2	3.7 ± 0.8	11.5 ± 0.7
	Pre-EMT	14.3	1462 ± 125	62 ± 1	14.2 ± 0.2	6.1 ± 0.1	7.3 ± 0.1	3.6 ± 0.2	11.5 ± 0.2
	EMT	4.3	1702 ± 135	62 ± 1	14.0 ± 0.3	6.0 ± 0.1	7.1 ± 0.1	3.3 ± 0.5	11.7 ± 0.4
	Post-EMT-A	3.3	1903 ± 180	58 ± 1	14.5 ± 0.3	6.2 ± 0.1	7.3 ± 0.1	3.5 ± 0.4	12.1 ± 0.4
	Post-EMT-B	2.3	2892 ± 227	55 ± 1	15.1 ± 0.2	6.4 ± 0.1	7.6 ± 0.1	3.8 ± 0.4	12.1 ± 0.4
	Post-EMT-C	1.8	2414 ± 235	56 ± 1	14.8 ± 0.4	6.5 ± 0.2	7.5 ± 0.1	3.5 ± 0.3	13.1 ± 0.5
	AW	3.7	88 ± 14	23 ± 5	16.7 ± 0.5	6.8 ± 0.2	8.6 ± 0.2	9.2 ± 0.5	8.3 ± 0.4
WestMED	EIW	11.4	364 ± 79	51 ± 5	17.0 ± 0.2	7.1 ± 0.1	8.8 ± 0.1	7.1 ± 0.4	9.8 ± 0.4
	WIW	6.9	170 ± 33	45 ± 5	17.6 ± 0.3	7.3 ± 0.1	9.1 ± 0.1	8.1 ± 0.4	9.6 ± 0.4
	A	9.3	1210 ± 156	67 ± 1	16.9 ± 0.2	7.0 ± 0.1	8.4 ± 0.1	4.8 ± 0.2	12.3 ± 0.2
	B	5.8	1632 ± 222	61 ± 2	16.5 ± 0.3	6.9 ± 0.2	8.3 ± 0.1	4.6 ± 0.4	11.8 ± 0.3
	C	0.7	2012 ± 300	56 ± 1	16.3 ± 0.6	6.6 ± 0.3	8.1 ± 0.3	4.2 ± 0.7	11.6 ± 0.8
	D11	0.7	2476 ± 357	55 ± 1	16.0 ± 0.5	6.5 ± 0.2	8.0 ± 0.2	4.2 ± 0.4	11.3 ± 0.6
	D14	5.4	2134 ± 160	56 ± 1	16.3 ± 0.2	6.6 ± 0.1	8.1 ± 0.1	4.3 ± 0.2	11.6 ± 0.3

Note: MAW: Modified Atlantic Water, LSW: Levantine Surface Water, LIW: Eastern Levantine Intermediate Water, CIW: Cretan Intermediate Water, AdMW: Middle Adriatic Water, AdDW: Adriatic Deep Water, Pre-EMT: Eastern Mediterranean Deep Water (EMDW) previous to the EMT, EMT: EMDW during the EMT, Post-EMT-A: EMDW after the EMT found in the Levantine basin, Post-EMT B: EMDW formed after the year 2003, Post-EMT-C: EMDW formed after the year 2007, AW: Atlantic Water, EIW: Eastern Intermediate Water formed in the Levantine Basin, WIW: Winter Intermediate Water, A: Western Mediterranean Deep Water (WMDW) formed prior to the year 2005, B: WMDW formed in winter 2004/5 in the Gulf of Lions, C: originated in winter 2004/5 with high influence of coastal shelf waters, D11: WMDW formed prior to the year 2011, D14: WMDW formed prior to the year 2014.

previously obtained x_{ij} values is performed. A system of n linear equations (one per sample) with m coefficients (one per WT) has to be solved for each variable N:

$$N_j = \sum_j x_{ij} \cdot \alpha_i \tag{3}$$

where α_i is the linear fitting parameter of water type i. The determination coefficient (R^2) and the standard deviation of the residuals (SD res) of this regression define the goodness of the fit.

Finally, to consider simultaneously the effect of mixing and biogeochemical processes on the distribution of FDOM variables, a term is added to Eq. (3) that models the non–conservative processes independent of the water type proportions. To do that, an additional explanatory chemical variable (N_2) is introduced to model the distribution of the response variable (N_1) as follows:

$$N_{1j} - \sum_j x_{ij} \cdot \alpha_{1i} = \beta \cdot \left(N_{2j} - \sum_j x_{ij} \cdot \alpha_{2i} \right) \tag{4}$$

Note that the term in the left represents the residuals of Eq. (3) for the response variable and the term in parenthesis in the right are the residuals of Eq. (3) for the explanatory variable. β is the fitting parameter of the relationship between N_1 and N_2, independent of water mass mixing, assuming that such a relationship is linear and homogeneous (i.e., β does not vary) in all the study area. This equation can be rearranged as follows:

$$N_{1j} = \sum_j x_{ij} \cdot (\alpha_{1i} - \beta \cdot \alpha_{2i}) + \beta \cdot N_{2j} \tag{5}$$

Therefore, a system of n linear equations (one per sample) with m + 1 unknowns (one per water type, $\alpha_{1i} - \beta \cdot \alpha_{2i}$, and the coefficient β) has to be solved. For further details please see Catalá et al. (2018).

3. Results

3.1. Fluorescent DOM components in the Mediterranean Sea

A 4–component model was obtained from the PARAFAC analysis (Fig. 2). Components 1, 2 and 4 have been already classified as humic–like (Coble, 1996, Stedmon et al., 2003). Component 1 corresponds to a mixture of Coble's (1996) peaks A (shorter excitation wavelength associated with general humic substances) and C (longer excitation wavelength linked to terrestrial humic substances) and component 2 to Coble's (1996) peak M, related with marine humic substances. Component 4 is close to Stedmon et al. (2003) peak E, which has been associated with soil fulvic acids. On the contrary, component 3 has been classified as protein–like, exhibiting its maximum fluorescence at the Ex/Em wavelength pair of 280/320 nm, which is in between Coble's (1996) peaks T and B. Therefore, this component represents a mixture of tryptophan– and tyrosine–like compounds.

Given that the PARAFAC components roughly match the classical fluorescence peak intensities at the Ex/Em wavelength pairs previously established by Coble (1996) and Stedmon et al. (2003), we decided to use the latter in order to allow direct comparison with previous studies.

3.2. Distribution of fluorescent DOM in the Mediterranean Sea

The three major humic–like peaks (A, C and M) presented very strong positive correlations among them (peak A vs peak M, $R^2 = 0.91$, $p < 0.0001$, n = 317, peak A vs peak C, $R^2 = 0.91$, $p < 0.0001$, n = 317 and peak C vs peak M $R^2 = 0.97$, $p < 0.0001$, n = 317). Thus, for simplicity, we will report only peak M results. Although peak E also exhibited positive correlations with the other humic-like peaks, they were much weaker (peak E vs peak A, $R^2 = 0.44$, $p < 0.0001$, n = 314, peak E vs peak C, $R^2 = 0.55$, $p < 0.0001$, n = 314 and peak E vs peak M $R^2 = 0.43$, $p < 0.0001$, n = 314). Therefore, we will present the results of peak E apart.

Fluorescence intensities of peak M ranged from 2 to 11 × 10^{-3} RU. Lower values were found at the surface layer with mean values (upper 100 m) of 4 ± 2 × 10^{-3} and 7 ± 2 × 10^{-3} RU for the EastMed and WestMed, respectively. Concerning water masses, in the EastMed the lowest intensities of peak M corresponded with LSW (archetype depth of 116 ± 21 m) with an archetype intensity of 5.5 ± 0.3 × 10^{-3} RU. On the other hand, the highest intensities were attributed to the

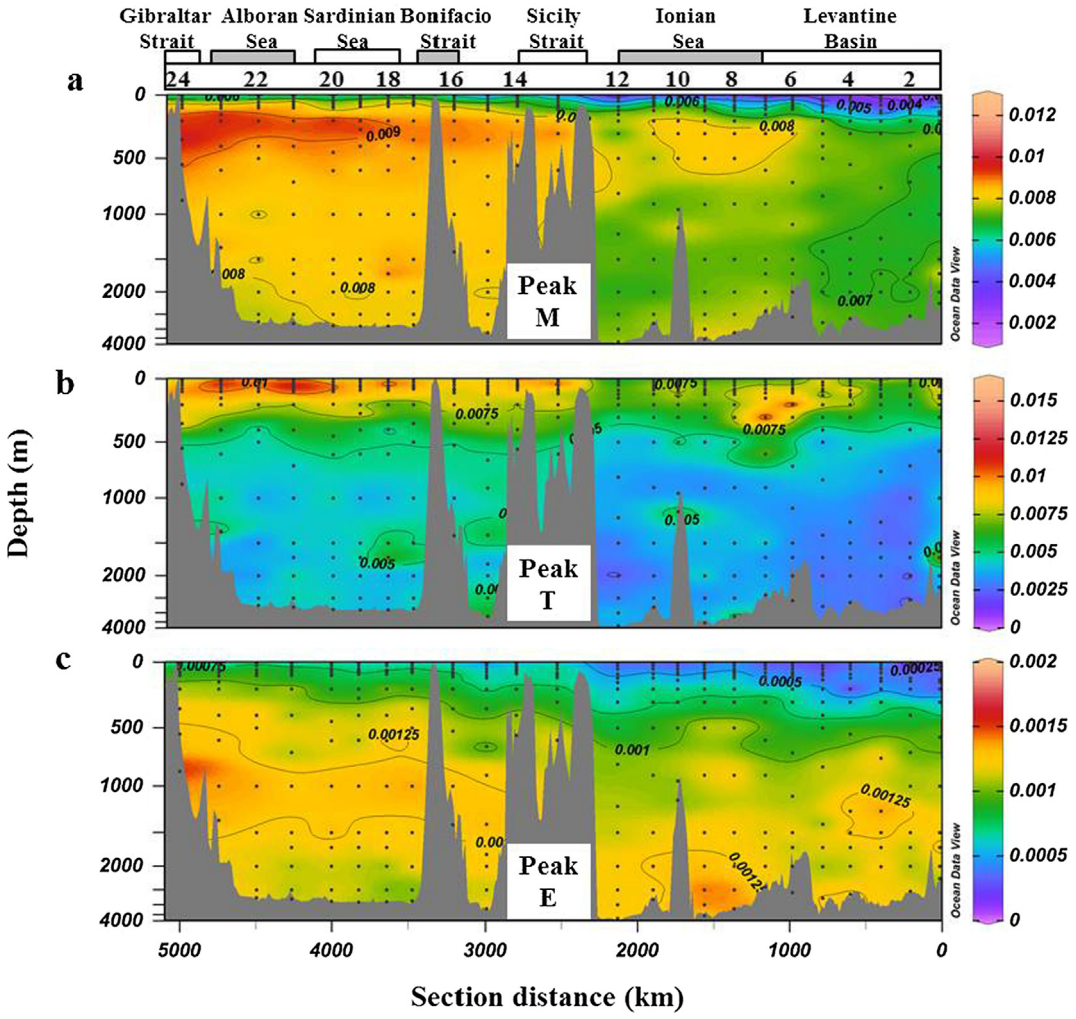

Fig. 3. Distribution of the fluorescence peaks. (a) Peak M (RU), (b) peak T (RU) and (c) peak E (RU) along the Mediterranean Sea. Numbers located on the top of the figure indicate the sample stations, which are depicted in Fig. 1. Figure created using ODV software (Schlitzer, 2017).

intermediate waters, characterized by maximum archetype values of $8.0 \pm 0.2 \times 10^{-3}$ RU. In the Levantine basin, peak M increased with depth up to about 200 m and then was kept constant through the water column until reaching the bottom. In the Ionian Sea, peak M showed higher intensities than in the Levantine basin, increasing down to the intermediate waters and maintaining almost constant through the water column below this depth (Fig. 3a and Fig. S2a). In the WestMed, peak M fluorescence increased from surface to intermediate waters where maximum intensities were recorded (red branch in Fig. 3a) and then decreased monotonically with depth. In this basin, maximum values were found in EIW and WIW (archetype depths of 364 ± 79 m and 170 ± 33 m, respectively) with archetype values of $8.8 \pm 0.1 \times 10^{-3}$ RU and $9.1 \pm 0.1 \times 10^{-3}$ RU, respectively (Table 1).

The basin-wide variability of protein-like substances will be described on basis of peak T measurements. Protein–like fluorescence ranged between 2 and 15×10^{-3} RU and, similarly to peak M fluorescence, exhibited higher intensities in the WestMed (Fig. 3b and Fig. S2b). Contrary to peak M, peak T showed higher intensities at the surface with mean values in the upper 100 m of $7 \pm 2 \times 10^{-3}$ and $10 \pm 2 \times 10^{-3}$ RU for the EastMed and WestMed, respectively. Peak T decreased through the water column, achieving minimum values at the bottom in both basins. In the EastMed, MAW and LSW presented an archetype intensity of $7.4 \pm 0.6 \times 10^{-3}$ and $7.6 \pm 0.8 \times 10^{-3}$ RU, respectively, significantly lower (t–test, $p < 0.05$, $\alpha = 0.05$) than AW in the WestMed, $9.2 \pm 0.1 \times 10^{-3}$ RU. These basin–wide differences in the upper layer can be easily recognised in Fig. 3b. In the intermediate layer of the EastMed, LIW presented significantly higher (t–test, $p < 0.05$, $\alpha = 0.05$) archetype peak T intensity than CIW ($7.5 \pm 0.3 \times 10^{-3}$ RU and $6.0 \pm 0.7 \times 10^{-3}$ RU, respectively). Analogously, in the WestMed, WIW presented slightly higher archetype peak T intensity than EIW ($8.1 \pm 0.4 \times 10^{-3}$ RU and $7.1 \pm 0.4 \times 10^{-3}$ RU, respectively). Comparison between the water masses of the intermediate layers in both basins at similar depths yielded no differences in the archetype intensities of peak T (Table 1). Regarding the deep waters, the mean archetype intensity of all EMDW varieties was $3.5 \pm 0.2 \times 10^{-3}$ RU, significantly lower (t–test, $p < 0.0001$, $\alpha = 0.05$) than WMDW average value ($4.4 \pm 0.3 \times 10^{-3}$ RU). The archetype intensities of peak T in the different deep water varieties were homogeneous inside each basin (Table 1).

Fluorescence intensities of peak E ranged from 1 to 15×10^{-4} RU, that is an order of magnitude lower than peaks M and T. Lower intensities were found at the surface layer (upper 100 m) with mean values of $4 \pm 2 \times 10^{-4}$ and $7 \pm 2 \times 10^{-4}$ RU for the EastMed and WestMed, respectively. In the epipelagic layer MAW presented significantly lower archetypal value ($5.5 \pm 0.7 \times 10^{-4}$ RU) than AW ($8.3 \pm 0.4 \times 10^{-4}$ RU) (t–test, $p < 0.001$, $\alpha = 0.05$). In the intermediate layer LIW exhibited a significantly lower archetypal value ($4.9 \pm 0.4 \times 10^{-4}$ RU) than EIW ($9.8 \pm 0.4 \times 10^{-4}$ RU) (t–test, $p < 0.0001$, $\alpha = 0.05$). In the bathypelagic layer, basin-scale differences were not evident (Fig. 3c), exhibiting mean archetype values of 12 ± 1 and $12.0 \pm 0.4 \times 10^{-4}$ RU, for the EastMed and WestMed, respectively (Table 1). Considering the deep water varieties of the

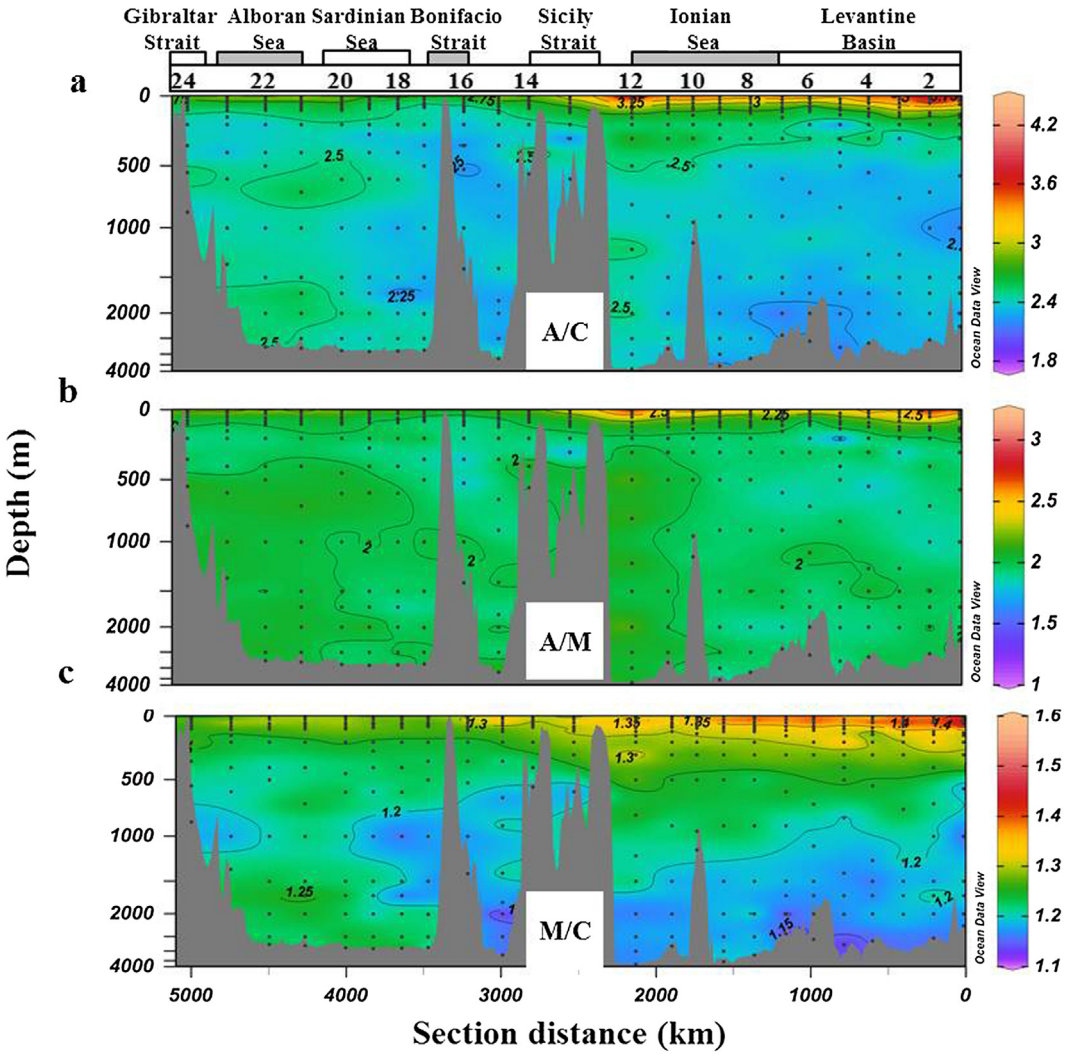

Fig. 4. Distribution of the fluorescence ratios: (a) peak A/C, (b) A/M and (c) M/C along the Mediterranean Sea. Numbers located on the top of the figure indicate the sample stations, which are depicted in Fig. 1. Figure created using ODV software (Schlitzer, 2017).

EastMed, Post-EMT-C (newest deep water mass) presented the highest archetypal value of peak E (13.1 $\pm$ 0.5 $\times$ 10^{-4} RU).

Despite the strong correlations ($R^2 > 0.91$) among the main humic-like peaks (A, C and M) shown at the beginning of this section, the distributions of the A/C, A/M and M/C ratios still retain a clear pattern with depth and basin: the highest values of the ratios are found in the surface layer of the EastMed (Fig. 4).

3.3. Results of GAMs analysis in the epipelagic waters of the Mediterranean Sea

To assess the drivers that dictate the distribution of the fluorescence peaks in the epipelagic layer of the MedSea we performed a GAM analysis. The model results indicated that > 88% of the variability of peaks A, C and M was explained by a combination of θ, AOU, Chl *a* and PHA. The main explanatory variables were θ, AOU and Chl *a* (Table 2), showing a positive linear relationship with AOU and Chl *a* and an inverse relationship with θ (Fig. 5a–c). Concerning peak E, the model explained 74% of the total variability, with θ, AOU and PHA as selected explanatory variables (Fig. 5d and Table 2). PHA was the better predictor of the variability of peak E with a shift from an inverse to a direct linear relationship. Peak E showed a positive linear relationship with AOU, similar to that observed with peaks A, C and M (Fig. 5a–c), nevertheless it showed an inverse relationship with θ. Regarding peak T, the total variance explained was significantly lower (31%) than for the humic–like peaks (Table 2). PHA and θ were the only two variables that contributed to explain the observed variability. PHA had a strong influence on the distribution of peak T with a shift from an inverse to a direct linear relationship at around $e^{12.5}$ ($=2.7 \times 10^5$) cell mL^{-1} (Fig. 5e). The explanatory power of θ was lower and showed a negative linear relationship with peak T.

In summary, while AOU is the major explanatory variable of the peaks A, C and M, peaks E and T were mostly explained by PHA.

3.4. Mixing and biogeochemical model results for the meso– and bathypelagic waters of the Mediterranean Sea

Fluorescence peaks presented strong linear correlations with water mass mixing proportions ($R^2 > 0.62$) (Table 3). Specifically, 73% of the variability of the intensity of peak M is explained by water mass mixing. It should be kept in mind that this multiple linear regression model with water type proportions retains not only the variability due to different initial concentrations at the formation area of each water type, but also the large scale mineralization from the formation area to the study section (Álvarez-Salgado et al., 2013; Catalá et al., 2018). Inclusion of a biogeochemical parameter as AOU in the multiple regression model improves the explained variance to 76%. In addition the SD of the residuals of the estimation improved by 5.8%. More

Table 2
Results of the Generalized Additive Models (GAMs) fitted to the fluorescence variables. Note that only statistically significant covariates were retained in the final formulations. SE = Standard Error; EDF = Estimated Degrees of Freedom; DE = Deviance Explained; N = number of data. See the main text for the variables and parameters descriptions. Note that Chl *a* fluorescence and Bacterial abundance (PHA) were ln-transformed.

Fluorescence variable	Parameter	Estimate (± SE)	EDF	t-value	F-value	P-value
Peak A	Intercept	13.01 (0.11)		123.6		< 0.0001
N = 160	θ		1.00		79.27	< 0.0001
DE = 87.9%	AOU		1.60		14.37	< 0.0001
	Chl *a*		1.80		14.65	< 0.0001
	PHA		1.98		13.61	< 0.0001
Peak C	Intercept	4.88 (0.05)		107		< 0.0001
N = 161	θ		1.12		69.23	< 0.0001
DE = 91.1%	AOU		1.00		52.45	< 0.0001
	Chl *a*		1.63		28.03	< 0.0001
	PHA		1.98		12.47	< 0.0001
Peak M	Intercept	6.32 (0.06)		103.1		< 0.0001
N = 161	θ		1.52		44.11	< 0.0001
DE = 89.2%	AOU		1.00		22.11	< 0.0001
	Chl *a*		1.42		24.99	< 0.0001
	PHA		1.95		8.67	0.0003
Peak E	Intercept	0.59 (0.01)		54.93		< 0.0001
N = 159	θ		1.84		7.62	0.0009
DE = 73.7%	AOU		1.67		8.99	0.0002
	PHA		1.97		30.86	< 0.0001
Peak T	Intercept	8.18 (0.15)		53.83		< 0.0001
N = 165	θ		1.00		3.89	0.05
DE = 31%	PHA		1.93		29.88	< 0.0001

importantly, a water mass mixing independent peak M/AOU ratio of 2.1 (± 0.4) × 10^{-5} RU μmol $O_2{}^{-1}$ kg was obtained (Table 3), suggesting a production of marine humic–like substances in parallel to water mass ageing. For the case of the protein–like peak T the variability explained by the water mass mixing model was slightly lower (62%) and the mixing–biogeochemical model barely reduced the SD of the residuals, but a significant ($p < 0.05$) water mass mixing independent peak T/AOU ratio of −3.7 (± 1.3) × 10^{-5} RU μmol $O_2{}^{-1}$ kg was obtained (Table 3). Contrary to the humic–like peak M, peak T/AOU ratio was negative, suggesting a decay of this fluorophore in parallel with water mass ageing. For peak E the mixing model explained 83% of the variability. The explained variance and the SD of the residuals did not improve when the mixing-biogeochemical model is applied but a significant ($p < 0.0001$) water mass mixing independent peak E/AOU ratio of 3 (± 1) × 10^{-6} RU μmol $O_2{}^{-1}$ kg (Table 3) is obtained.

Considering the two basins independently, the variance explained of the fluorescence peaks using the mixing model was significantly lower in the WestMed than in the EastMed, except for peak T (Table 3). Regarding the mixing–biogeochemical model, the EastMed presented significantly higher water mass mixing-independent peak M/AOU (t–test, $p < 0.001$, $\alpha = 0.05$) and slightly higher peak E/AOU ratios of 5 (± 1) × 10^{-5} and 5 (± 3) × 10^{-6} μmol $O_2{}^{-1}$ kg, respectively compared to the WestMed of 1.6 (± 0.4) × 10^{-5} and 2 (± 1) × 10^{-6} μmol $O_2{}^{-1}$ kg, respectively. The water mass mixing independent peak T/AOU in the EastMed, −8 (± 3) × 10^{-5} μmol $O_2{}^{-1}$ kg, was more negative than in the WestMed, −2.7 (± 1.2) × 10^{-5} μmol $O_2{}^{-1}$ kg, due to the oligotrophy of the EastMed. This is related to the fact that in the EastMed 66% of the oxygen consumption is due to the DOC mineralization, however in the WestMed the DOC mineralization accounted for only 24% (Catalá et al. 2018). This is, about 2.7 times (66%/24%) more influence of DOC than sinking POC en the EastMed. Alike for DOC, given that peak T represents a labile fraction of DOC, it is expected that this influence should be even higher. In fact, it is about 3 times (8/2.7).

4. Discussion

All fluorophores found in this work were previously reported in the literature (Coble, 1996, Stedmon et al., 2003; Catalá et al., 2015a; Pitta et al., 2017, 2019). The PARAFAC components found in the MedSea compares to those found in the global ocean by Catalá et al. (2015a) (Fig. 2). Component 1 corresponded to peaks A + C and component 2 to peak M in both studies. Our component 3 (protein–like, mixture of tryptophan and tyrosine) corresponded to component 4 (related to tyrosine) of Catalá et al. (2015a). However, our component 4 matched to humic–like peak E previously found in coastal areas (Stedmon et al., 2003, Stedmon and Markager, 2005) but not in the open ocean (e.g. Jørgensen et al., 2011; Kowalczuk et al., 2013; Catalá et al., 2015a). In the Mediterranean Sea peak E was already found in the mixing zone of the Dardanelles Strait and the North Aegean Sea, which is an area of strong terrestrial influences due to river discharge into the Black Sea (Pitta et al., 2017). The fact that we observed this component also in the open MedSea points to the impact of continental runoff in the distal zone of this relatively small and enclosed basin.

4.1. FDOM drivers in oligotrophic epipelagic waters

Photobleaching is the likely reason behind the low fluorescence intensities of the humic–like fluorophores (peaks A, C, M and E) in epipelagic waters as compared with deep waters of the MedSea (Kouassi and Zika, 1992; Moran et al., 2000; Mopper et al., 2015; Pitta et al., 2017, 2019). Humic-like substances contain aromatic structures that are prone to undergo decomposition into colourless smaller molecules. Furthermore, fluorescence intensity was lower in the epipelagic EastMed than in the WestMed, because the AW, that enters the MedSea through the Strait of Gibraltar and displaces eastwards towards the Levantine basin, experiences progressive photodegradation during its route. Although all humic–like substances undergo photodegradation, peak A was much less sensitive than peaks M, C and E (Fig. 4). Note that in the case of peak A, the excitation wavelength (250 nm) is outside the natural solar spectrum (> 295 nm) and, therefore, the effect of photobleaching should be secondary (Del Vecchio and Blough, 2002). In the case of peaks M, C and E, the excitation wavelengths (320, 340 and 440 nm, respectively) are within the photochemically active part of the natural solar spectrum (Fichot and Benner, 2011).

On the contrary, protein–like fluorescence was higher at the epipelagic layer and declined with depth in agreement with Jørgensen et al. (2011), who suggested a labile or semilabile nature of these compounds linked to primary production. In the epipelagic layer, protein–like fluorescence presented lower intensity in the EastMed despite DOC concentrations were higher there (Catalá et al. 2018). This combination of higher DOC but lower protein–like fluorescence intensity is likely associated to the ultra–oligotrophy of the EastMed that could preclude a regular functioning of the microbial loop (Thingstad et al., 1997). Following these authors, we propose that in the EastMed phytoplankton exude organic matter depleted in nitrogen or structurally different than that formed in the WestMed. In addition, we also propose that prokaryotes are not able to decompose DOM because of the extremely low values of nutrients in these surface waters (0.1 ± 0.3 and 1.0 ± 0.5 μmol kg^{-1} $NO_3{}^-$ and 0.01 ± 0.01 and 0.04 ± 0.07 μmol kg^{-1} $HPO_4{}^{-2}$ for the first 100 m of the EastMed and WestMed, respectively). Note that this fact does not mean that the accumulated compounds are refractory, but just that the microbial communities somehow are not able to use them. Conversely, in the WestMed the higher nutrient concentrations, transported by the surface AW entering from the Atlantic Ocean through the Strait of Gibraltar,

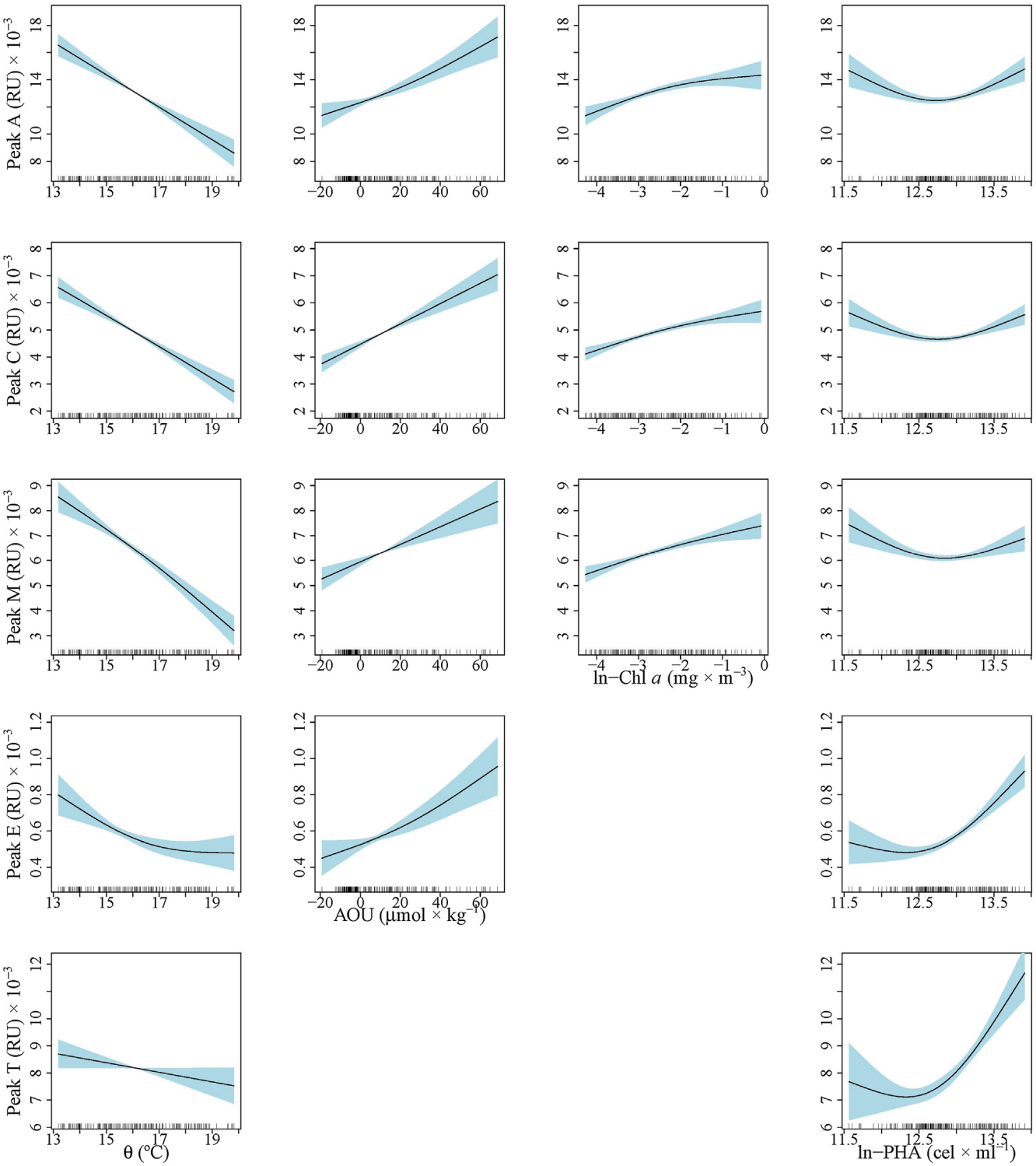

Fig. 5. Partial plots of the additive effects of the physical, chemical and biological covariates on the FDOM parameters after fitting Generalized Additive Models. (a) Peak A, (b) Peak C, (c) peak M, (d) peak E and (e) peak T. Rugs on x-axis indicate the distribution of the data.

stimulate the primary production and the accumulation of protein–like compounds by means of phytoplanktonic exudation processes. Note that the AW in the Gulf of Cadiz (West of the Strait Gibraltar) presented lower fluorescence intensity of peak T than in the MedSea (data not shown). This result suggests that peak T is produced in the MedSea instead of being transported from the Atlantic Ocean.

The GAM analysis showed that in the epipelagic layer the distribution of peak M fluorescence were addressed mainly by 4 variables (Fig. 5c): (i) AOU, which is a proxy of the net community respiration (i.e. the community respiration minus the autotrophic oxygen production) integrated over the time elapsed since the water was last in contact with the atmosphere, (ii) Chl *a* concentration, which is indicative of autotrophic biomass and it is in agreement with the findings of marine humic–like substances generated by phytoplankton (Romera-Castillo et al., 2010; Fukuzaki et al., 2014), and (iii) θ, which apart from being related to stratification, can be partly considered as a proxy to solar

Table 3
Parameters of the linear mixing (Eq. (3)) and mixing-biogeochemical (Eq. (5)) models. R^2, determination coefficient; SD res, standard deviation of the residuals of the estimation; % SD reduction, percentage of reduction of the SD res of the mixing biogeochemical as compared with the corresponding mixing model; β, fitting parameter of the relationship between N_1 and N_2 independent of the mixing; SE(β), standard error of the estimation of β; *p*, significance level of the estimation of β. Results are presented for meso– and bathypelagic samples of the whole MedSea and for the EastMed and WestMed, separately.

N_1	N_2	R^2	SD res	%SD reduction	β	SE(β)	*p*	n
MedSea								
AOU		0.88	7.8					233
PHA		0.78	88,518					240
Peak A		0.72	0.001					240
Peak C		0.77	0.0004					240
Peak M		0.73	0.00052					240
Peak T		0.62	0.00149					240
Peak E		0.83	0.00012					237
Peak A	AOU	0.74	0.00097	4.9%	0.000033	0.000009	0.0001	233
Peak C	AOU	0.79	0.0004	7.1%	0.000019	0.000003	0.0000	233
Peak M	AOU	0.76	0.00049	5.8%	0.000021	0.000004	0.0000	233
Peak T	AOU	0.63	0.00148	0.7%	−0.000037	0.000013	0.05	233
Peak E	AOU	0.83	0.00012	–	0.000003	0.000001	0.0001	231
EastMed								
AOU		0.96	4.4					130
PHA		0.85	51,696					134
Peak A		0.64	0.001					134
Peak C		0.69	0.00043					134
Peak M		0.59	0.00058					134
Peak T		0.55	0.00167					134
Peak E		0.86	0.00012					131
Peak A	AOU	0.64	0.001	–	–	–	Ns	130
Peak C	AOU	0.73	0.00040	7%	0.00004	0.00001	0.0000	130
Peak M	AOU	0.64	0.00055	5.2%	0.00005	0.00001	0.0001	130
Peak T	AOU	0.56	0.00164	1.8%	−0.00008	0.00003	0.02	130
Peak E	AOU	0.86	0.00012	–	0.000005	0.000003	0.0001	128
WestMed								
AOU		0.72	10.6					103
PHA		0.73	119,700					106
Peak A		0.26	0.001					106
Peak C		0.40	0.0004					106
Peak M		0.50	0.00042					106
Peak T		0.71	0.00124					106
Peak E		0.64	0.00012					106
Peak A	AOU	0.36	0.001	–	0.00004	0.00001	0.0001	103
Peak C	AOU	0.51	0.00035	12.5%	0.000015	0.000003	0.0000	103
Peak M	AOU	0.59	0.00037	9.5%	0.000016	0.000004	0.0000	103
Peak T	AOU	0.72	0.00123	0.8%	−0.000027	0.000012	0.02	103
Peak E	AOU	0.63	0.00012	–	0.000002	0.000001	0.0001	103

irradiation, and therefore linked to photodegradation processes. Peak T was mainly controlled by PHA (Fig. 5e and Table 2). To a lesser extent, θ also controlled the distribution of peak T. In this case, it should not be related with photodegradation processes since peak T is less sensitive to photobleaching. However, it could be due to the enhancement of biological processes with increasing temperatures. The distribution of peak E was driven mainly by PHA and to a lesser extent by AOU and θ. In this case, contrary to peak T, θ is mainly related with photodegradation processes. Note that although AOU is negative at the surface because autotrophic oxygen production exceeds community respiration, there was not any change in the shape of the relationship of any FDOM peak and AOU when this variable changes from net community production (AOU < 0) to net community respiration (AOU > 0) (Figs. 5 and 6). Therefore, it was not necessary to analyse both set of samples separately. Likewise for the MedSea, Catalá et al. (2016) found that AOU and Chl *a* were the main environmental drivers of the humic–like distributions for the global ocean. For the amino–acid like components these authors reported salinity and depth as the main explanatory variables and PHA showing a lesser influence on the tyrosine distribution and salinity and AOU for tryptophan distribution.

4.2. FDOM drivers in meso– and bathypelagic waters

Maximum fluorescence intensities of peak M were found in the intermediate layers, corresponding to CIW in the EastMed and to WIW and EIW in the WestMed matching with the highest AOU values. These results are in agreement with the hypothesis of humic–like compounds being produced by microbes as by–products during bioavailable organic matter mineralization (Kramer and Herndl, 2004, Nieto-Cid et al., 2006; Yamashita and Tanoue, 2008; Jørgensen et al., 2011; Catalá et al., 2015a, Zhao et al., 2017). The lower fluorescence intensity of peak M in the intermediate layers of the EastMed compared to the WestMed is related to the ultra–oligotrophic EastMed presenting lower heterotrophic production and enzymatic activities (Luna et al., 2012). Regarding the deep water masses, they presented different behaviour depending on the basin. While deep waters of the WestMed showed the expected positive trend between peak M and AOU (red circles in Fig. 6a), deep waters of the EastMed showed a negative relationship between both variables (white circles in Fig. 6a) and also a counter-intuitive positive relationship with DOC (white circles on the left in Fig. 6d). In the WestMed, deep water mass varieties presented different ages but the same area of formation and, therefore, equivalent peak M intensities at the formation time. They also presented similar DOC concentrations (red circles on the left in Fig. 6d). However, deep water masses of the EastMed presented different peak M values at their formation time depending on the formation site. In this case, we hypothesized that the area of formation have a larger influence than the subsequent alteration due to biogeochemical processes in the final

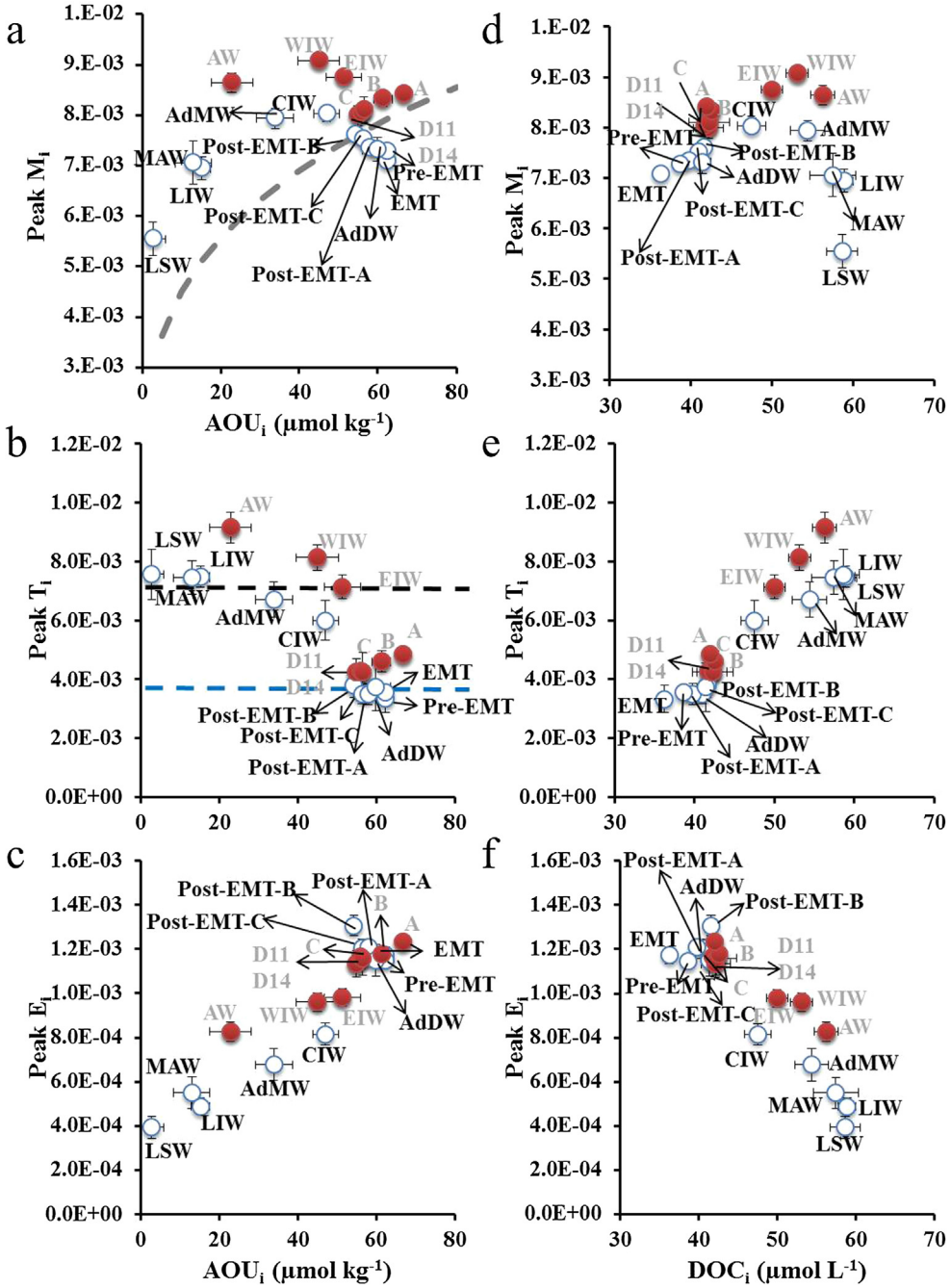

Fig. 6. Relationships of archetype fluorescence peak intensities with archetype apparent oxygen utilization (AOU_i, µmol kg^{-1}) and archetype dissolved organic carbon (DOC_i, µmol kg^{-1}). (a) archetype peak M (peak M_i, RU), (b) archetype peak T (peak T_i) and (c) archetype peak E (peak E_i), *versus* AOU_i.. (d) peak M_i, (e) peak T_i, and (f) peak E_i, *versus* DOC_i). Error bars represent the standard deviation of the estimated archetypal values. Red and white circles represent samples of the WestMed and EastMed, respectively. The acronyms of the water masses are explained in Table 1.The dashed grey line in panel (a) represents the regression curve found in Catalá et al. (2015a) for the global ocean. The dashed black and blue lines in panel (b) represent the mean archetypes values found in Catalá et al. (2015a) in the Atlantic Ocean (black) and in the Indian /Pacific Oceans (blue). (For interpretation of the references to colour in this figure legend, the reader is referred to the web version of this article.)

intensity of peak M. Specifically, fluorescence intensity of peak M was significantly higher (t–test, $p < 0.005$, $\alpha = 0.05$) in Post–EMT–B and –C water masses (archetype AOU = 55 ± 1 and 56 ± 1 µmol kg^{-1}, respectively) than in the water masses formed during the EMT (archetype AOU = 62 ± 1 µmol kg^{-1}) in spite of being formed earlier and presenting lower archetype AOU. While Post–EMT–B and –C water masses were formed in the Adriatic Sea, EMT was originated in the Aegean Sea (Roether et al., 1996). On the other hand, in the deep waters of the WestMed, the water mass WMDW–A (archetype AOU, 67 ± 1 µmol kg^{-1}) presented significantly higher (t–test, $p < 0.05$, $\alpha = 0.05$) peak M fluorescence than WMDW–D14 variety (archetype AOU = 56 ± 1 µmol kg^{-1}), as WMDW–A was the oldest WMDW in this basin, formed prior to WMT (before 2004/5; (López-Jurado et al., 2005; Schroeder et al., 2016). Compared to the global ocean (grey dashed line in Fig. 6a), the subsurface and intermediate waters (AOU < 40 µmol kg^{-1}) of the MedSea are characterised by a higher peak M fluorescence for the same AOU. For the deep waters (AOU > 40 µmol kg^{-1}), whereas in the WestMed the peak M-AOU relationship follows the global ocean equation (Fig. 6a), in the EastMed the varieties of EMDW are characterised by a lower peak M intensity for the same AOU than in the global ocean To do these comparisons, we translated the fluorescence intensity of the PARAFAC component 2 from Catalá et al. (2015a) into the corresponding peak M intensities.

Regarding peak T in the EastMed, LIW presented the highest intensity of the water masses that coexist in the mesopelagic layer, probably because it is the shallowest and youngest intermediate water of the EastMed. The archetype fluorescence intensity of LIW was similar to MAW and LSW, which are centred at similar archetype depths. In addition, when considering deep water masses, all varieties hosted similar peak T intensities. Similarly, in the WestMed, AW was the water mass with the highest peak T intensity due to its shallowness and, therefore, proximity to the primary production layer. Down in the

mesopelagic layer, WIW presented higher intensity than EIW because the former was more recently formed in the Gulf of Lions and the Balearic Sea. However, EIW was originated in the Levantine basin and mixed with the surrounding water masses in its route westwards (EMDW, CIW and WIW, the latter is present in the western part of the Strait of Sicily) and then, once in the WestMed, EIW was further mixed with WIW and WMDW (Catalá et al., 2018). Regarding the WMDW varieties, they presented an unexpected positive relationship between peak T and AOU (four red circles in bottom right Fig. 6b). However this increase is not observed in the Peak T – DOC relationship (red circles in bottom Fig. 6e). The susceptibility of peak T of being affected by peak–tailing from humic–like compounds or small organic acids fluorescing near the peak T region (Stubbins et al., 2014) is a feasible reason that may cause those differences. To compare the AOU–peak T relationship in the MedSea to that found in the global ocean by Catalá et al. (2015a), we calculated the mean archetype values for the Atlantic and the Indian and Pacific Ocean from the data reported by Catalá et al. (2015a). Then we translated from the fluorescence intensity of PARAFAC component 3 and the corresponding peak T intensity for the global ocean leading to the black and blue dashed lines in Fig. 6b. MedSea samples with AOU $< 50\,\mu mol\,kg^{-1}$ were parallel to the Atlantic Ocean samples (higher peak T fluorescence intensities). On contrary, MedSea deep water samples (AOU $> 50\,\mu mol\,kg^{-1}$) followed the Indian and Pacific pattern (with lower peak T fluorescence intensities).

Peak E presented lower fluorescence intensities than the other peaks, either humic– or protein–like, as previously observed by Pitta et al. (2017), as well as a different distribution compared to peak M (Fig. 3a, c). While peak M presented significant differences between the EastMed and WestMed, peak E was homogeneously distributed. Similarly to peak M, peak E in the WestMed deep waters showed a positive relationship with AOU (red circles in Fig. 6c) and in the EastMed the relationship was negative (white circles on the top right Fig. 6c). Likewise in the case of peak M these changes were also observed in the DOC–peak E relationship for the EastMed samples but not for the WestMed (Fig. 6f).

Regarding the mixing model and considering both basins independently, the variance explained of fluorescence peaks were significantly lower in the WestMed than in the EastMed. This result indicates that water mass mixing was more influential in the EastMed because of its ultra–oligotrophy. In addition, the water mass mixing independent peak M/AOU ratio obtained in the MedSea, 2.1 (± 0.4) × 10^{-5} RU µmol $O_2{}^{-1}$ kg, is not significantly different from the value obtained by Catalá et al. (2015a) for the global ocean during the circumnavigation Malaspina, 1.9 (± 0.1) × 10^{-5} RU µmol $O_2{}^{-1}$ kg. This result indicates that the efficiency of conversion of these marine humic–like compounds from microbial respiration was similar in the MedSea and the global ocean. The water mass mixing independent peak E/AOU ratio 3 (± 1) × 10^{-6} RU µmol $O_2{}^{-1}$ kg, also suggests a production of peak E fluorescence in parallel to cumulative microbial respiration, but an order of magnitude lower than for peak M. However, as peak E has been associated with soil fulvic acids (Stedmon et al., 2003), the production of this terrestrial material in the deep MedSea as a by–product of respiration processes is unexpected. Likely, the explanation to this positive relationship between peak E and AOU could be the enhancement of the fluorescence intensity of the existing terrestrial source material (soil fulvic acid) by further chemical or microbial transformations (Andrew et al., 2013) rather than its autochthonous production. Alternatively, it could be argued that peak E does not represent exclusively soil fulvic acids but it would be produced in the ocean too.

Finally, in this work we have reported a positive relationship between peak M and AOU (Table 3). However, in the companion paper by Catalá et al. (2018), it was observed a negative relationship between a_{325} and AOU, indicating a consumption of these coloured compounds. Since peak M absorb at a_{325}, it should be expected that both peak M and a_{325} had parallel trends with AOU as it was already observed for the global ocean (Catalá et al., 2015a, 2015b). However, the trends of peak M and a_{325} were opposite in the MedSea. These results suggest that in the oligotrophic MedSea the CDOM fraction absorbing at a_{325} nm but not emitting fluorescence is consumed at a higher rate than the production of the fluorescent fraction, resulting in an unexpected net inverse relationship.

5. Conclusions

In the epipelagic layer of the MedSea, AOU, Chl *a* and θ explained most of the variability of the humic–like fluorescence, suggesting a dominant influence of microbial food web respiration and photobleaching in the distribution of these compounds. On the contrary, the variability of protein–like fluorescence was largely explained by PHA. In the meso– and bathypelagic layers, the combination of water mass mixing and basin scale mineralization explained better the variability of peaks A, C, M and E (> 72%) than the variability of peak T (62%). Considering both basins independently, the explained variance was better in the EastMed due to its extreme oligotrophy. Regarding the deep water masses, while FDOM peaks dynamics in the WestMed was mostly driven by ageing, in the EastMed knowledge of EMDW formation areas, in the Adriatic or the Aegean Sea, was relevant to explain the distributions. Estimation of water mass independent ratios of FDOM peaks with AOU revealed that the production of peak M by net microbial respiration (peak M/AOU ratio) was similar in the MedSea than in the open global ocean. Furthermore, the fact that contrary to the peak M/AOU ratio, the a_{325}/AOU ratio was negative (Catalá et al., this issue), indicates that in the particular case of the MedSea the consumption of the non fluorescent fraction of CDOM that absorbs at 325 nm exceeds the production of the fluorescent fraction represented by peak M.

Acknowledgements

The authors are grateful to the Captain, crew, technicians and scientists aboard the R/V Sarmiento de Gamboa for their support during the cruise. We specially thank to M.J. Pazó and V. Vieitez for DOC and nutrient measurements and H. SanLeón–Bartolomé for dissolved oxygen. This work was funded by the project HOTMIX (grant number CTM2011–30010–C02 01–MAR and 02–MAR), co–financed with FEDER funds. A.M.M.–P. was funded by a predoctoral fellowship (reference BES–2012–056175) from the Spanish Ministry of Economy, Industry and Competitiveness and the project MODMED from CSIC (PIE, 201730E020). M.N.–C. was partially supported by the project FERMIO (MINECO, CTM2014–57334–JIN), co–financed with FEDER funds.

T.S.C. was supported by a predoctoral fellowship from the Ministry of Education, Culture y Sports (Ref. AP2009–2138), the project FOMEM (Spanish Research Council, CSIC–PIE No 201030E130) and a postdoctoral contract jointly financed by the project CGL2014–52362R of the Spanish Ministry of Economy and Competitiveness and FEDER funds and the University of Granada.

Contributions

A.M.M.–P., M.N.–C. and X.A.A.–S. designed the research. A.M.M.–P., M.N.–C., T. S. C., M.A., M.E., X.A. A.–S., J.A. participated in the field work. M. A. applied the water mass analysis. J.O. executed the GAM analysis. T.S.C executed the PARAFAC modelling. A.M.M.–P and X.A.A.–S wrote the first draft manuscript, which was complemented by significant contributions of all co–authors.

Appendix A. Supplementary material

Supplementary data to this article can be found online at https://

doi.org/10.1016/j.pocean.2018.10.019.

References

Álvarez-Salgado, X.A., Nieto-Cid, M., Álvarez, M., Pérez, F.F., Morin, P., Mercier, H., 2013. New insights on the mineralization of dissolved organic matter in central, intermediate, and deep water masses of the northeast North Atlantic. Limnol. Oceanogr. 58, 681–696. https://doi.org/10.4319/lo.2013.58.2.0681.

Anderson, L.A., 1995. On the hydrogen and oxygen content of marine phytoplankton. Deep Sea Res. Part I Oceanogr. Res. Pap. 42, 1675–1680. https://doi.org/10.1016/0967-0637(95)00072-E.

Andrew, A.A., Del Vecchio, R., Subramaniam, A., Blough, N.V., 2013. Chromophoric dissolved organic matter (CDOM) in the Equatorial Atlantic Ocean: optical properties and their relation to CDOM structure and source. Mar. Chem. 148, 33–43. https://doi.org/10.1016/j.marchem.2012.11.001.

Aparicio, F.L., Nieto-Cid, M., Calvo, E., Pelejero, C., López-Sanz, À., Pascual, J., Salat, J., Sánchez-Pérez, E.D., De La Fuente, P., Gasol, J.M., Marrasé, C., 2017. Wind–induced changes in the dynamics of fluorescent organic matter in the coastal NW Mediterranean. Sci. Total Environ. 609, 1001–1012. https://doi.org/10.1016/j.scitotenv.2017.07.170.

Bergamasco, A., Malanotte-Rizzoli, P., 2010. The circulation of the Mediterranean Sea: a historical review of experimental investigations. Adv. Oceanogr. Limnol. 1, 11–28. https://doi.org/10.1080/19475721.2010.491656.

Bro, R., 1997. PARAFAC. Tutorial and applications. Chemom. Intell. Lab. Syst. 38, 149–171. https://doi.org/10.1016/S0169-7439(97), 00032-4.

Catalá, T.S., Reche, I., Fuentes-Lema, A., Romera-Castillo, C., Nieto-Cid, M., Ortega-Retuerta, E., Calvo, E., Álvarez, M., Marrasé, C., Stedmon, C.A., Álvarez-Salgado, X.A., 2015a. Turnover time of fluorescent dissolved organic matter in the dark global ocean. Nat. Commun. 6, 5986. https://doi.org/10.1038/ncomms6986.

Catalá, T.S., Reche, I., Álvarez, M., Khatiwala, S., Guallart, E.F., Benítez-Barrios, V.M., Fuentes-Lema, A., Romera-Castillo, C., Nieto-Cid, M., Pelejero, C., Fraile-Nuez, E., Ortega-Retuerta, E., Marrasé, C., Álvarez-Salgado, X.A., 2015b. Water mass age and aging driving chromophoric disolved organic matter in the dark global ocean. Global Biogeochem. Cycles 29. https://doi.org/10.1002/2014GB005048.

Catalá, T.S., Álvarez-Salgado, X.A., Otero, J., Iuculano, F., Companys, B., Horstkotte, B., Romera-Castillo, C., Nieto-Cid, M., Latasa, M., Morán, X.A.G., Gasol, J.M., Marrasé, C., Stedmon, C.A., Reche, I., 2016. Drivers of fluorescent dissolved organic matter in the global epipelagic ocean. Limnol. Oceanogr. 61, 1101–1119. https://doi.org/10.1002/lno.10281.

Catalá, T.S., Martínez-Pérez, A.M., Nieto-Cid, M., Álvarez, M., Otero, J., Emelianov, M., Reche, I., Arístegui, J., Álvarez-Salgado, X.A., 2018. Dissolved Organic Matter (DOM) in the open Mediterranean Sea. I. Basin wide distribution and drivers of chromophoric DOM. Prog. Oceanogr. 165, 35–51. https://doi.org/10.1016/j.pocean.2018.05.002.

Coble, P.G., 1996. Characterization of marine and terrestrial DOM in seawater using excitation–emission matrix spectroscopy. Mar. Chem. 51, 325–346. https://doi.org/10.1016/0304-4203(95), 00062-3.

Coble, P.G., 2007. Marine optical biogeochemistry: the chemistry of ocean color. Chem. Rev. 107, 402–418. https://doi.org/10.1021/cr050350.

Coble, P.G., Lead, J., Baker, A., Reynolds, D.M., Spencer, R.G.M., 2014. Aquatic Organic Matter Fluorescence, Cambridge Environmental Chemistry Series. Cambridge University Press, Cambridge. https://doi.org/10.1017/CBO9781139045452.

Cyr, F., Tedetti, M., Besson, F., Beguery, L., Doglioli, A.M., Petrenko, A.A., Goutx, M., 2017. A new glider–compatible optical sensor for dissolved organic matter measurements: test case from the NW Mediterranean sea. Front. Mar. Sci. 4, 89. https://doi.org/10.3389/fmars.2017.00089.

Del Vecchio, R., Blough, N.V., 2002. Photobleaching of chromophoric dissolved organic matter in natural waters: kinetics and modeling. Mar. Chem. 78, 231–253. https://doi.org/10.1016/S0304-4203(02)00036-1.

Dickson, R.R., Brown, J., 1994. The production of North Atlantic Deep Water: sources, rates, and pathways. J. Geophys. Res. 99, 12319–12341. https://doi.org/10.1029/94JC00530.

Fichot, C.G., Benner, R., 2011. A novel method to estimate DOC concentrations from CDOM absorption coefficients in coastal waters. Geophys. Res. Lett. 38, L03610. https://doi.org/10.1029/2010GL046152.

Fukuzaki, K., Imai, I., Fukushima, K., Ishii, K.-I., Sawayama, S., Yoshioka, T., 2014. Fluorescent characteristics of dissolved organic matter produced by bloom–forming coastal phytoplankton. J. Plankton Res. 36, 685–694. https://doi.org/10.1093/plankt/fbn015.

Gonnelli, M., Galletti, Y., Marchetti, E., Mercadante, L., Retelletti Brogi, S., Ribotti, A., Sorgente, R., Vestri, S., Santinelli, C., 2016. Dissolved organic matter dynamics in surface waters affected by oil spill pollution: results from the Serious Game exercise. Deep Res. Part II Top. Stud. Oceanogr. 133, 88–99. https://doi.org/10.1016/j.dsr2.2016.05.027.

Grasshoff, K., Kremling, K., Ehrhardt, M., 1999. Determination of nutrients. In: Brügmann, L., Kremling, K. (Eds.), Methods of Seawater Analysis. WILEY–VCH Verlag GmbH, pp. 159–228.

Holm-Hansen, O., Lorenzen, C.J., Holmes, R.W., Strickland, J.D.H., 1965. Fluorometric determination of chlorophyll. J. du Cons. 30, 3–15. https://doi.org/10.1093/icesjms/30.1.3.

Jørgensen, L., Stedmon, C.A., Kragh, T., Markager, S., Middelboe, M., Søndergaard, M., 2011. Global trends in the fluorescence characteristics and distribution of marine dissolved organic matter. Mar. Chem. 126, 139–148. https://doi.org/10.1016/j.marchem.2011.05.002.

Kouassi, A.M., Zika, R.G., 1992. Light–induced destruction of the absorbance property of dissolved organic matter in seawater. Toxicol. Environ. Chem. 35, 195–211. https://doi.org/10.1080/02772249209357816.

Kowalczuk, P., Tilstone, G.H., Zabłocka, M., Röttgers, R., Thomas, R., 2013. Composition of dissolved organic matter along an Atlantic Meridional Transect from fluorescence spectroscopy and Parallel Factor Analysis. Mar. Chem. 157, 170–184. https://doi.org/10.1016/j.marchem.2013.10.004.

Kramer, G.D., Herndl, G.J., 2004. Photo– and bioreactivity of chromophoric dissolved organic matter produced by marine bacterioplankton. Aquat. Microb. Ecol. 36, 239–246. https://doi.org/10.3354/ame036239.

Langdon, C., 2010. Determination of dissolved oxygen in seawater by Winkler titration using the amperometric technique. GO–SHIP repeat hydrography manual: a collection of expert reports and guidelines. IOC/IOCCP, Paris.

Laruelle, G.G., Roubeix, V., Sferratore, A., Brodherr, B., Ciuffa, D., Conley, D.J., Dürr, H.H., Garnier, J., Lancelot, C., Le Thi Phuong, Q., Meunier, J.-D., Meybeck, M., Michalopoulos, P., Moriceau, B., Ní Longphuirt, S., Loucaides, S., Papush, L., Presti, M., Ragueneau, O., Regnier, P., Saccone, L., Slomp, C.P., Spiteri, C., Van Cappellen, P., 2009. Anthropogenic perturbations of the silicon cycle at the global scale: key role of the land–ocean transition. Global Biogeochem. Cycles 23, GB4031. https://doi.org/10.1029/2008GB003267.

López-Jurado, J., Gonzalez-Pola, C., Velez-Belchi, P., 2005. Observation of an abrupt disruption of the long–term warming trend at the Balearic Sea, western Mediterranean Sea, in summer 2005. Geophys. Res. Lett. 32, L24606. https://doi.org/10.1029/2005GL024430.

Luna, G.M., Bianchelli, S., Decembrini, F., De Domenico, E., Danovaro, R., Dell'Anno, A., 2012. The dark portion of the Mediterranean Sea is a bioreactor of organic matter cycling. Global Biogeochem. Cycles 26, GB2017. https://doi.org/10.1029/2011GB004168.

Mopper, K., Kieber, D.J., Stubbins, A., 2015. Chapter 8 – Marine Photochemistry of Organic Matter: Processes and Impacts, In: Biogeochemistry of Marine Dissolved Organic Matter. pp. 389–450. https://doi.org/10.1016/B978-0-12-405940-5.00008.

Moran, M.A., Sheldon, W.M., Zepp, R.G., 2000. Carbon loss and optical property changes during long–term photochemical and biological degradation of estuarine dissolved organic matter. Limnol. Oceanogr. 45, 1254–1264. https://doi.org/10.4319/lo.2000.45.6.1254.

Murphy, K.R., Butler, K.D., Spencer, R.G.M., Stedmon, C.A., Boehme, J.R., Aiken, G.R., 2010. Measurement of dissolved organic matter fluorescence in aquatic environments: an interlaboratory comparison. Environ. Sci. Technol. 44, 9405–9412. https://doi.org/10.1021/es102362t.

Murphy, K.R., Stedmon, C.A., Graeber, D., Bro, R., 2013. Fluorescence spectroscopy and multi–way techniques. PARAFAC. Anal. Methods 5, 6557–6566. https://doi.org/10.1039/c3ay41160e.

Nelson, N.B., Siegel, D.A., 2013. The global distribution and dynamics of chromophoric dissolved organic matter. Ann. Rev. Mar. Sci. 5, 447–476. https://doi.org/10.1146/annurev-marine-120710-100751.

Nelson, N.B., Gauglitz, J.M., 2016. Optical signatures of dissolved organic matter transformation in the global gcean. Front. Mar. Sci. 2, 118. https://doi.org/10.3389/fmars.2015.00118.

Nieto-Cid, M., Álvarez-Salgado, X.A., Pérez, F.F., 2006. Microbial and photochemical reactivity of fluorescent dissolved organic matter in a coastal upwelling system. Limnol. Oceanogr. 51, 1391–1400. https://doi.org/10.4319/lo.2006.51.3.1391.

Para, J., Coble, P.G., Charrière, B., Tedetti, M., Fontana, C., Sempéré, R., 2010. Fluorescence and absorption properties of chromophoric dissolved organic matter (CDOM) in coastal surface waters of the northwestern Mediterranean Sea, influence of the Rhône River. Biogeosciences 7, 4083–4103. https://doi.org/10.5194/bg-7-4083-2010.

Pitta, E., Zeri, C., Tzortziou, M., Mousdis, G., Scoullos, M., 2017. Seasonal variations in dissolved organic matter composition using absorbance and fluorescence spectroscopy in the Dardanelles Straits – North Aegean Sea mixing zone. Cont. Shelf Res. 149, 82–95. https://doi.org/10.1016/j.csr.2016.07.013.

Pitta, E., Zeri, C., Tzortziou, M., Rijkenberg, M.J.A., 2019. Transformations of dissolved organic matter in the Marmara Sea traced by its optical signature. J. Mar. Syst. 189, 1–11. https://doi.org/10.1016/j.jmarsys.2018.09.001.

Powley, H.R., Krom, M.D., Van Cappellen, P., 2016. Circulation and oxygen cycling in the Mediterranean Sea: Sensitivity to future climate change. J. Geophys. Res. Ocean. 121, 8230–8247. https://doi.org/10.1002/2016JC012224.

Roether, W., Manca, B.B., Klein, B., Bregant, D., Georgopoulos, D., Beitzel, V., Kovacevic, V., Luchetta, A., 1996. Recent changes in eastern Mediterranean deep waters. Science 271, 333–335. https://doi.org/10.1126/science.271.5247.333.

Romera-Castillo, C., Sarmento, H., Álvarez-Salgado, X.A., Gasol, J.M., Marrasé, C., 2010. Production of chromophoric dissolved organic matter by marine phytoplankton. Limnol. Oceanogr. 55, 446–454. https://doi.org/10.4319/lo.2010.55.1.0446.

Romera-Castillo, C., Álvarez-Salgado, X.A., Galí, M., Gasol, J.M., Marrasé, C., 2013. Combined effect of light exposure and microbial activity on distinct dissolved organic matter pools. A seasonal field study in an oligotrophic coastal system (Blanes Bay, NW Mediterranean). Mar. Chem. 148, 44–51. https://doi.org/10.1016/j.marchem.2012.10.004.

Sánchez-Pérez, E.D., Marín, I., Nunes, S., Aparicio, F.L., Fernández-González, L., Peters, F., Pujo-Pay, M., Conan, P., Marrasé, C., 2016. Aerosol inputs affect the optical signatures of dissolved organic matter in NW Mediterranean coastal waters. Sci. Mar. 80 (4), 437–446. https://doi.org/10.3989/scimar.04318.20B.

Santinelli, C., 2015. DOC in the Mediterranean Sea. In: Hansell, D.A., Carlson, C.A. (Eds.), Biogeochemistry of Marine Dissolved Organic Matter, second ed. Academic Press, Boston, pp. 579–608.

Schlitzer, R., Ocean Data View, http://odv.awi.de, 2017.

Schneider, A., Tanhua, T., Roether, W., Steinfeldt, R., 2014. Changes in ventilation of the Mediterranean Sea during the past 25 year. Ocean Sci. 10, 1–16. https://doi.org/10.

5194/os-10-1-2014.
Schroeder, K., Chiggiato, J., Bryden, H.L., Borghini, M., Ben Ismail, S., 2016. Abrupt climate shift in the Western Mediterranean Sea. Sci. Rep. 6, 23009. https://doi.org/10.1038/srep2300.
Stedmon, C.A., Markager, S., 2005. Resolving the variability in dissolved organic matter fluorescence in a temperate estuary and its catchment using PARAFAC analysis. Limnol. Oceanogr. 50 (2), 686–697. https://doi.org/10.4319/lo.2005.50.2.0686.
Stedmon, C.A., Markager, S., Bro, R., 2003. Tracing dissolved organic matter in aquatic environments using a new approach to fluorescence spectroscopy. Mar. Chem. 82, 239–254. https://doi.org/10.1016/S0304-4203(03), 00072-0.
Stedmon, C.A., Bro, R., 2008. Characterizing dissolved organic matter fluorescence with parallel factor analysis: a tutorial. Limnol. Oceanogr. Methods 6, 572–579. https://doi.org/10.4319/lom.2008.6.572.
Stedmon, C.A., Nelson, N.B., 2015. Chapter 10 – The Optical Properties of DOM in the Ocean. In: Hansell, D.A., Carlson, C.A. (Eds.), Biogeochemistry of Marine Dissolved Organic Matter. Elsevier, pp. 481–508. https://doi.org/10.1016/B978-0-12-405940-5.00010-8.
Stubbins, A., Lapierre, J.-F., Berggren, M., Prairie, Y.T., Dittmar, T., Del Giorgio, P.A., 2014. What's in an EEM? Molecular signatures associated with dissolved organic fluorescence in boreal Canada. Environ. Sci. Technol. 48, 10598–10606. https://doi.org/10.1021/es502086e.
Thingstad, T.F., Hagström, A., Rassoulzadegan, F., 1997. Accumulation of degradable DOC in surface waters: is it caused by a malfunctioning microbial loop? Limnol. Oceanogr. 42, 398–404. https://doi.org/10.4319/lo.1997.42.2.0398.
Tomczak, M., Large, D.G.B., 1989. Optimum multiparameter analysis of mixing in the thermocline of the eastern Indian Ocean. J. Geophys. Res. Ocean. 94, 16141–16149. https://doi.org/10.1029/JC094iC11p16141.
UNESCO, 1985. The International System of Units (SI) in oceanography. UNESCO Tech. Paper. Mar. Sci. 45, 1–124.
UNESCO, 1986. Progress on oceanographic tables and standards 1983–1986. Work and recommendations of UNESCO/SCOR/ICES/IAPSO joint panel UNESCO. Tech. Pap. Mar. Sci. 50, 1–59.
Wood, S.N., 2006. Generalized Additive Models: An Introduction with R. Chapman & Hall/CRC, London.
Yamashita, Y., Tanoue, E., 2008. Production of bio–refractory fluorescent dissolved organic matter in the ocean interior. Nat. Geosci. 1, 579–582. https://doi.org/10.1038/ngeo279.
Yamashita, Y., Hashihama, F., Saito, H., Fukuda, H., Ogawa, H., 2017. Factors controlling the geographical distribution of fluorescent dissolved organic matter in the surface waters of the Pacific Ocean. Limnol. Oceanogr. 62, 2360–2374. https://doi.org/10.1002/lno.10570.
Zeri, C., Beşiktepe, T., Giannakourou, A., Krasakopoulou, E., Tzortziou, M., Tsoliakos, D., Pavlidou, A., Mousdis, G., Pitta, E., Scoullos, M., Papathanassiou, E., 2014. Chemical properties and fluorescence of DOM in relation to biodegradation in the interconnected Marmara-North Aegean Seas during August 2008. J. Mar. Syst. 135. https://doi.org/10.1016/j.jmarsys.2013.11.019.
Zhao, Z., Gonsior, M., Luek, J., Timko, S., Ianiri, H., Hertkorn, N., Schmitt-Kopplin, P., Fang, X., Zeng, Q., Jiao, N., Chen, F., 2017. Picocyanobacteria and deep–ocean fluorescent dissolved organic matter share similar optical properties. Nat. Commun. 8, 15284. https://doi.org/10.1038/ncomms15284.